

Realisation of sub-wavelength a single dimple using 193 nm wavelength photonic nano jet

Q.A. Al-Jarwany^{1,4}, A.F. Mohammed^{1,5}, A.O. Hamza^{1,6}, J-S G. Bouillard^{1,3}, A.M. Adawi^{1,3}, N. Pamme^{2,3}, and C.D. Walton^{1,3}

¹Department of Physics and Mathematics, University of Hull, HU6 7RX, UK.

²Department of Chemistry, University of Hull, HU6 7RX, UK.

³G. W. Gray Centre for Advanced Materials, University of Hull, HU6 7RX, UK.

⁴Material Engineering College, University of Babylon, Babylon, Iraq.

⁵Applied Physics Department, University of Technology, Baghdad, Iraq.

⁶Department of Physics, College of Science, Salahaddin University-Erbil, Iraq.

Abstract:

There are many areas of research that benefit sub wavelength tight focussing. We report experimental and computational results of a laser irradiated microsphere localised on an SU-8 substrate. A single pulse from an ArF excimer laser ($\lambda = 193$ nm) was used to generate a photonic nano jet (PNJ). Subsequently the PNJ was used to produce a dimple cavity in SU-8. Atomic force microscopy (AFM) was employed to determine dimple geometry which corresponded to a diameter of 150 ± 10 nm FWHM and a depth of 130 ± 10 nm. Finite difference time domain (FDTD) calculations were carried out to simulate the propagation of 193 nm radiation through the microsphere. Experimental results and simulations were in close agreement conforming that the electric field is tightly focussed by the microsphere. Finite Element Method (FEM) simulations were also carried out to calculate the laser induced temperature rise of SU-8 in the region beneath the micro-sphere. These FEM simulations predict a temperature of 775 K which is above the boiling point of SU-8 (480 K). We briefly

discuss the ejection mechanism of the microsphere in terms of the increase in temperature of the underlying SU-8. **They key finding is... c**

Keywords: microsphere, photonic nano-jet, laser

1.0 Introduction

Tight focusing of laser radiation continuous to find novel and wide ranging scientific and engineering applications. They range from high spatial resolution fluorescence microscopy [1], increasing the irradiance for high power laser welding and laser cutting [2], recording information in optical data storage [3], to the realisation of high electric field gradients in optical trapping [4–6] [7].

A classic text related to focussing is the book titled *Waves in Focal Regions*, by Stamnes [29]. Research in this area began with Ignatowsky investigating diffraction properties of light that passes through an arbitrary aperture [30,31]. The diffraction problem was re-derived by Richards and Wolf [32] and later by Wolf [33]. The latter work applied Debye Kirchoff integrals, sometimes shortened to Debye integrals, to calculate the electric field in a focal region of an aplanatic optical system. Since these early studies focal regions continue to be an area of active research [34].

Within the photonics community various unconventional methods have been adopted to focus light including self-assembly of micrometre and nanometre-sized dielectric spheres. Under appropriate conditions well organised microsphere arrays have been produced and subsequently irradiated using laser radiation. [8,9]. Laser microsphere lithography has been reported using short pulse nanosecond KrF excimer laser radiation emitting at a wavelength of 248 nm [10,11] and at longer wavelengths using femto-second laser radiation emitting at a wavelength of 800 nm [11, 12]. As the optical absorption of dielectric materials tends to

increase with decreasing laser wavelength, the power transported through a microsphere results in a concomitant decrease in optical transmission. However, with careful selection of the microsphere material, microsphere diameter, laser wavelength and surrounding medium it is possible to calculate losses and also the position of the focal region. In this work a reduced transparency at 193 nm UV wavelengths is not necessarily problematic per se as the optical path length is relatively short across the diameter of the microsphere.

An interesting phenomenon associated with focusing of light through small dielectric microspheres is the generation of photonic nano jets (PNJs). Electromagnetic radiation in the form of light is confined spatially in the lateral direction and extends significantly along the beam propagation direction [14] [15]. Confinement of optical radiation has been observed not only in dielectric microspheres but also with optical fibres that have been re-shaped taking on the form of fibre tapers and spherical ball shapes at the distal end [16]. Fibre axicons [17,18] and other geometrical re-shaped fibres also serve as useful tools for focussing and spatially confining light. Delivering light along fibre waveguides is highly applicable for use in microfluidic devices [19]. It is sometimes desirable to build small and compact optical trapping systems for micro-fluidic applications and novel beam delivery systems are sort after. Conventional optical trapping systems typically manipulate objects that have a refractive index greater than the surrounding fluid, for example, polystyrene beads in water. However, in biological and medical fields, cells have low refractive indices that is frequently lower than the surrounding liquid. In such cases the optical trapping force is associated with an inverted refractive index contrast and such cells are trapped in the low intensity region referred to as dark traps. Cell trapping in the low intensity dark region is advantageous as the dark trap reduces potential cell damage cells [17]. Recently there has been a surge of activity in opto- photoporation for trapping and modification of cell membranes [20]. Cell membranes serve a multitude of functions and provide a tough physical barrier separating

intracellular and extracellular fluids. Being able to overcome and to controllably penetrate cell membranes whilst maintaining cell viability is a sought-after goal in drug delivery, gene therapy and personalised medicine. The use of small dielectric spheres that are capable of forming tightly focussed needle-like light may open up novel biomedical and biophysical applications. In this respect PNJs emitted from microspheres suspended in fluids that attach to cells [9] and microspheres fused on optical fibres for delivery of light may become useful tools for cell membrane disruption [16]. It is therefore of interest to quantify and optimise tightly focussed PNJs. By their definition PNJs have small lateral extent and various experimental techniques are available for characterising their shape and size. Small focal regions associated with focused Gaussian laser beams have been characterised using so called knife-edge measurements [21], and Z-scan methods [22]. However, more recently, single fluorescent molecules have been used to measure the structure of laser beam focal regions [4,23–26]. The latter technique is becoming extremely useful especially as new types of nanoparticles having high quantum efficiencies are being synthesised. Similarly, scanning near-field optical microscopy (SNOM) experiments consisting of sub-10 nm diameter fluorescent particles have been used to resolve the fine structure in focal regions [27]. These experimental characterisation techniques are experimentally challenging and therefore computational simulations compliment focal region characterisation.

In this work, we adopt experimental and computational investigations of the PNJ produced with 193 nm radiation from an ArF laser. We adopt an indirect focal spot measurement method to record a PNJ by measuring the material modification of a dimple formed in a SU-8 photo-resist. AFM to measure have been used to measure the profile of the underlying SU-8 photoresist. We note however this is an indirect method of spot size measurement which may overestimate the actual size of PNJ. The degree of overestimation will be dependent on the temperature of the SU-8 layer as mass will be lost when the temperature of the SU-8 is above

its boiling point. As the underlying substrate temperature will influence mass transport we calculate the temperature of SU-8 using Finite Element Method (FEM) using the software COMSOL™. Similarly, Finite Difference Time Domain (FDTD) simulations have been carried out using the software Lumerical™ to quantify the size of the focal region that has been produced by a microsphere. FDTD simulations are extremely valuable as they enable one to engineer the geometric extent of focal regions associated with PNJs. Similarly, FEM simulations of the temperature rise of SU-8 can be used to interpret mechanisms that are associated with ejection of microspheres when irradiated by laser radiation [28].

2.0 Microsphere Adhesion and Detachment

Although we are primarily interested in optical field enhancement and the realisation of small laser processed features, it is also informative to consider the force of adhesion and ejection of microspheres supported on an SU-8 substrate. Adhesion of particulates to substrates is also of interest from a laser cleaning perspective [36]. Small contaminating particles adhere strongly to surfaces. As the particle size decreases it becomes increasingly difficult to remove. Lasers used for laser cleaning have proven useful in this area. In these experiments a 1 μm diameter SiO₂ microsphere is supported on spun coated SU-8. Adhesion between the sphere and substrate is primarily associated with Van der Waals forces which can be calculated using equation (1).

$$F_1 = \frac{hr}{8\pi z^2} \quad (1)$$

where, r , z and h are the microsphere radius, separation between the sphere and substrate and material-dependent Lifshitz-Van der Waals constant respectively. The adhesion force is dependent to some extent on the compliance of the SU-8 substrate. As the microsphere

embeds and deforms the substrate the contact area is increased. Taking this into consideration we have an additional force term given by equation (2).

$$F_2 = \frac{h\delta^2}{8\pi z^3} \quad (2)$$

where, δ is the radius of the contact area. Addition of these terms gives an estimate of the total force of adhesion.

$$F_T = \frac{hr}{8\pi z^2} + \frac{h\delta^2}{8\pi z^3} \quad (3)$$

Observation of equation (3) highlights the importance of accurately quantifying the microsphere-interface separation distance, z , and hence this highlights the importance of surface roughness at interfaces. Using equation (3) the calculated adhesion force corresponds to $F_T = 280$ nN for a $1 \mu\text{m}$ diameter microsphere. This compares with the gravitational force acting on the particle of $F_g = 130$ pN. Hence, there is a relatively strong adhesion force between a small microsphere and the SU-8 substrate [35, 36]. It is informative to consider conditions that lead to ejection of the microsphere. We assume that the SiO_2 microsphere is optically transparent at 193 nm and the main propagation losses are those associated with reflection, a total of $\sim 10\%$ from both interfaces. Absorption losses inside the microsphere are minimal, partly due to the low optical absorption coefficient for SiO_2 at 193 nm and the short optical path length set by the $1 \mu\text{m}$ diameter particle. Knowledge of the energy absorbed by the substrate allows one to calculate the thermal expansion and concomitant acceleration of the substrate when a laser pulse is absorbed. Excimer laser pulse durations are short, typically tens of nanoseconds, and transfer of energy results in very large rates of change in temperature, typically $\sim 10^9 \text{ Ks}^{-1}$. Several mechanisms can oppose the adhesion force and result in detachment of the microsphere from the substrate. When the laser fluence beneath the microsphere is sufficiently this can result in melting of the substrate and the boiling point

may be exceeded. This may result in ablation and evaporation of substrate species which in turn contribute to the transfer of momentum to the microsphere. At high laser fluence plume expansion and gas dynamics may play a significant role in momentum transfer of substrate species and hence ejection of the microsphere. Equally important is thermal expansion of the underlying substrate. Fluence enhancement caused by focusing of 193 nm radiation will inevitably increase the temperature beneath the microsphere which leads to thermal expansion and displacement H of the substrate [36],

$$H = \alpha' \left[(1 - R_s) \frac{F}{\rho_s C_s} \right] \quad (4)$$

where α' is the coefficient of thermal expansion. Inserting corresponding numerical values; $F = 1.045 \text{ Jcm}^{-2}$, $\alpha' = 52 \times 10^{-6} \text{ K}^{-1}$, density $\rho_s = 1.2 \text{ g.cm}^{-3}$, and specific heat $C_s = 1.5 \text{ J.g}^{-1}\text{K}^{-1}$, we can estimate the displacement and corresponding acceleration, a . Due to the short laser pulse duration, $\tau = 12 \text{ ns}$ the acceleration of the substrate is significant and can be estimated from using

$$a = \frac{H}{\tau^2} \quad (5)$$

Utilization of short and ultrashort laser pulses result in very large substrate accelerations and is one reason why lasers have been used successfully for laser cleaning. Considering a time-dependent absorption of energy as is the case for excimer lasers one can calculate the displacement of the substrate [37, 38].

$$Z_s(t) = S_0 \frac{\beta_3 A_0}{C_s \rho_s} \int_0^t \frac{I(t-t_1) dt_1}{1 + \frac{4\chi t_1}{r_0^2}} \times \int_0^\infty \alpha_c dz \left[1 - \sqrt{\pi} \zeta e^{\zeta^2} \text{erfc}(\zeta) \right] F(z, t_1) \quad (6)$$

$$F(z,t) = \frac{1}{2} e^{\alpha_c^2 \chi t} \left\{ e^{\alpha_c z} \operatorname{erfc} \left[\alpha_c \sqrt{\chi t} + \frac{z}{2\sqrt{\chi t}} \right] + e^{-\alpha_c z} \operatorname{erfc} \left[\alpha_c \sqrt{\chi t} - \frac{z}{2\sqrt{\chi t}} \right] \right\} \quad (7)$$

where $F(z,t)$ represents an expression for spatio-temporal distribution of the laser pulse and α_c is the absorption coefficient. Using equation (6) and (7) and a corresponding value of the optical field enhancement, S_0 the substrate displacement, Z_s can be calculated.

3.0 Optical Field Enhancement.

Dielectric microspheres can be used to focus light and hence amplify an incident laser fluence. Consequently, absorption of tightly focused light may result in heating of a material and thermal expansion. As we have eluded the temperature beneath the microsphere is an important quantity as it contributes to ejection of the microsphere and formation of the dimple feature. Optical enhancement and focussing are dependent on the refractive power of the microsphere. Similarly, light scattering caused by surface roughness and imperfections may result in optical aberrations that reduce the optical enhancement factor. In the first instance one can simply calculate optical field enhancement for an un-aberrated optical system. The focal spot size can be estimated from the radius of microsphere, R , and the refractive index of the refracting microsphere. Using ray caustics we calculate the focal spot size [37] using

$$\omega = R \sqrt{\frac{(4-n^2)^3}{27n^4}} \quad (8)$$

where n is the refractive index of the microsphere at the corresponding wavelength. A simple and expedient approach of estimating the optical field enhancement is to consider the ratio between the intensity of the focussed beam I_t to the intensity of the incident beam I_0 .

$$\frac{I_t}{I_0} = \frac{a^2}{\omega^2} \approx \frac{27n^4}{(4-n^2)^3} \quad (9)$$

Equation 9 is a useful approximation for calculating optical enhancement however we note that it does not take into account Fabry-Perot type interference between the sphere and the underlying substrate. The spatial location of the high intensity focal region produced by the microsphere is dependent on optical aberrations and depolarisation. These effects becoming more influential as the numerical aperture increases. FDTD using the software Lumerical™ is used and described in chapter four.

We adopt semi-analytical equations first introduced by Richards and Wolf (R-W) [32] to calculate the electric field components, (E_x , E_y and E_z), inside the focal region at points, $P(r_p, \theta_p, \phi_p)$ [32].

$$E_x(r_p, \theta_p, \phi_p) = -iA(I_0 + I_2 \cos 2\phi_p) \quad (10)$$

$$E_y(r_p, \theta_p, \phi_p) = -iAI_2 \sin 2\phi_p \quad (11)$$

$$E_z(r_p, \theta_p, \phi_p) = -iAI_1 \cos \phi_p \quad (12)$$

where r_p , θ_p and ϕ_p are polar coordinates and I_0, I_1, I_2 are the corresponding functions used in the orthogonal electric field components

$$I_0 = I_0(kr_p, \theta_p, \alpha) = \int_0^\alpha \cos^{\frac{1}{2}} \theta \sin \theta (1 + \cos \theta) J_0(kr_p \sin \theta \sin \theta_p) e^{ikr_p \cos \theta \cos \theta_p} d\theta \quad (13)$$

$$I_1 = I_1(kr_p, \theta_p, \alpha) = \int_0^\alpha \cos^{\frac{1}{2}} \theta \sin^2 \theta J_1(kr_p \sin \theta \sin \theta_p) e^{ikr_p \cos \theta \cos \theta_p} d\theta \quad (14)$$

$$I_2 = I_2(kr_p, \theta_p, \alpha) = \int_0^\alpha \cos^{\frac{1}{2}} \theta \sin \theta (1 - \cos \theta) J_2(kr_p \sin \theta \sin \theta_p) e^{ikr_p \cos \theta \cos \theta_p} d\theta \quad (15)$$

α is the angular sine-aperture of the refracting element, k is the wave number, and

$A = kfl_0/2 = \pi fl_0/\lambda$ is a constant where λ is wavelength and f is the lens focal length. We

return to these equations when we discuss the correlation between the focal region and dimple formation in the modified SU-8.

4.0 Finite Difference Time Domain Simulations

FDTD simulations were carried out to calculate the electric field distribution and optical enhancement of a dielectric microsphere in contact with SU-8 using software by Lumerical™ version 8.19.1522. Calculations were restricted to two spatial dimensions (x - z), where x is a transverse direction and z is the direction of the incident beam normal to the SU-8 substrate [28-30]. The size of the 2D computational domain was set at $1.5 \times 2.5 \mu\text{m}$ and the corresponding mesh elements were set to 2 nm square. In the simulations a $1 \mu\text{m}$ diameter SiO_2 microsphere was positioned onto a flat surface that represented SU-8. To do this we assign the refractive index of the SiO_2 microsphere to $n_{ms} = 1.56 + i0.00152$ (at a wavelength of 193 nm) [42]. The refractive index for the medium surrounding the sphere was set at $n_m = 1$ and the refractive index of the SU-8 substrate was set to $n_{sub} = 1.8 + i0.006$ [43]. The boundary conditions were implemented by introducing a perfect matching layer (PML) to prevent unwanted reflections re-entering the computational domain. Calculations terminated when the electric field decayed to 10^{-5} of its original value.

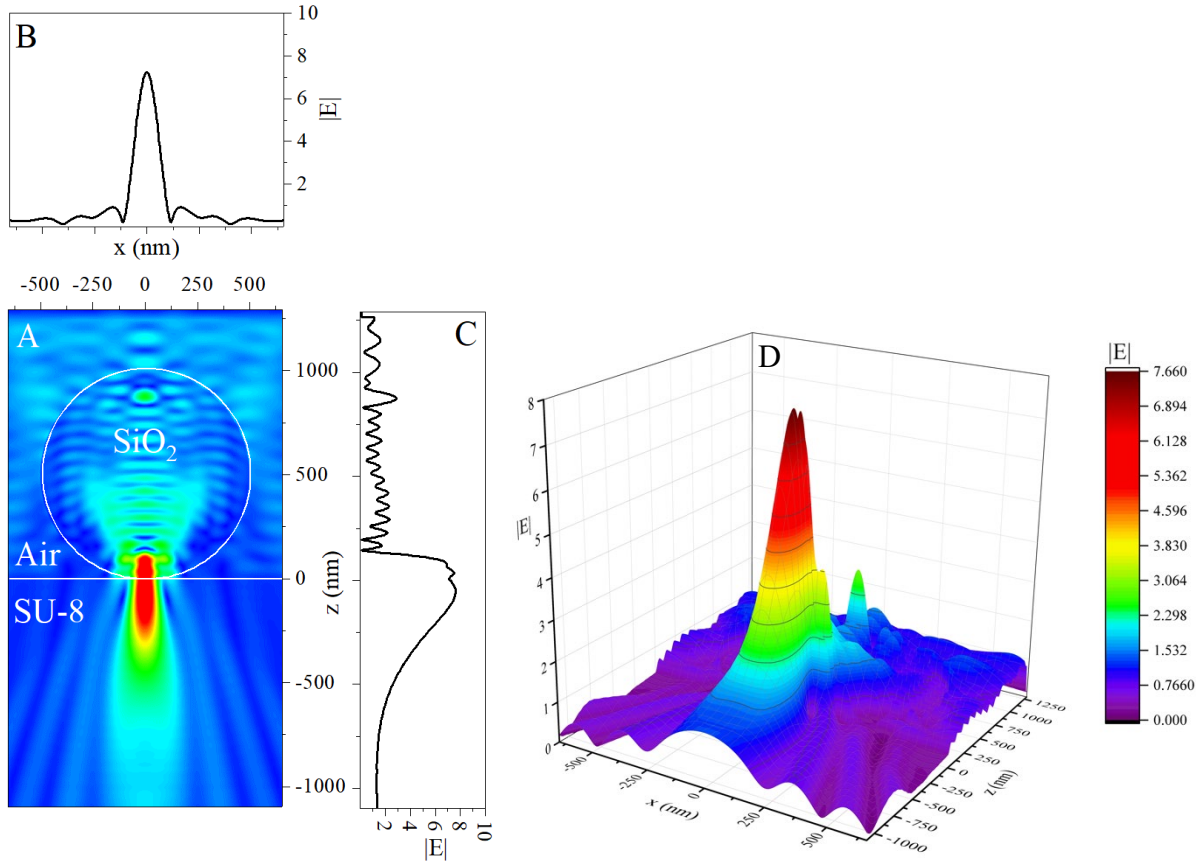


Fig. 1 (A) Simulated electric field in x - z plane for laser radiation at 193 nm propagation through a $1\mu\text{m}$ microsphere using linearly polarised light in the x direction and the wave propagates in the z -direction. A microsphere is positioned on a flat SU-8 surface. (B) Spatial cross-section of the simulated data through location of the peak intensity of the focussed PNJ. (C) Spatial cross-section of the peak intensity along the beam propagation direction, z . (D) 3D plot of the intensity of the focal region.

FDTD calculations were performed for visualisation purposes and to predict the spatial location of the focal region. Figures 1 and 2 illustrate the electric field $|E|$ and intensity $|E|^2$ calculations for 193 nm laser radiation incident onto a SU-8 substrate. It is clear from the simulations that the SiO_2 spherical particle focuses 193 nm radiation inside the SU-8 layer. From simulations we identify the peak position of the intensity along the z -direction which is located 180 nm away from the underside of the microsphere. From FDTD simulations we calculate an optical enhancement of the intensity of 40. This compares with a value of 41.6

from equation (9). From Fig 1.A, it can be seen the length of PNJ close to 300 nm underneath the silica particle. Fig 2 below shows similar results for the intensity $|E|^2$.

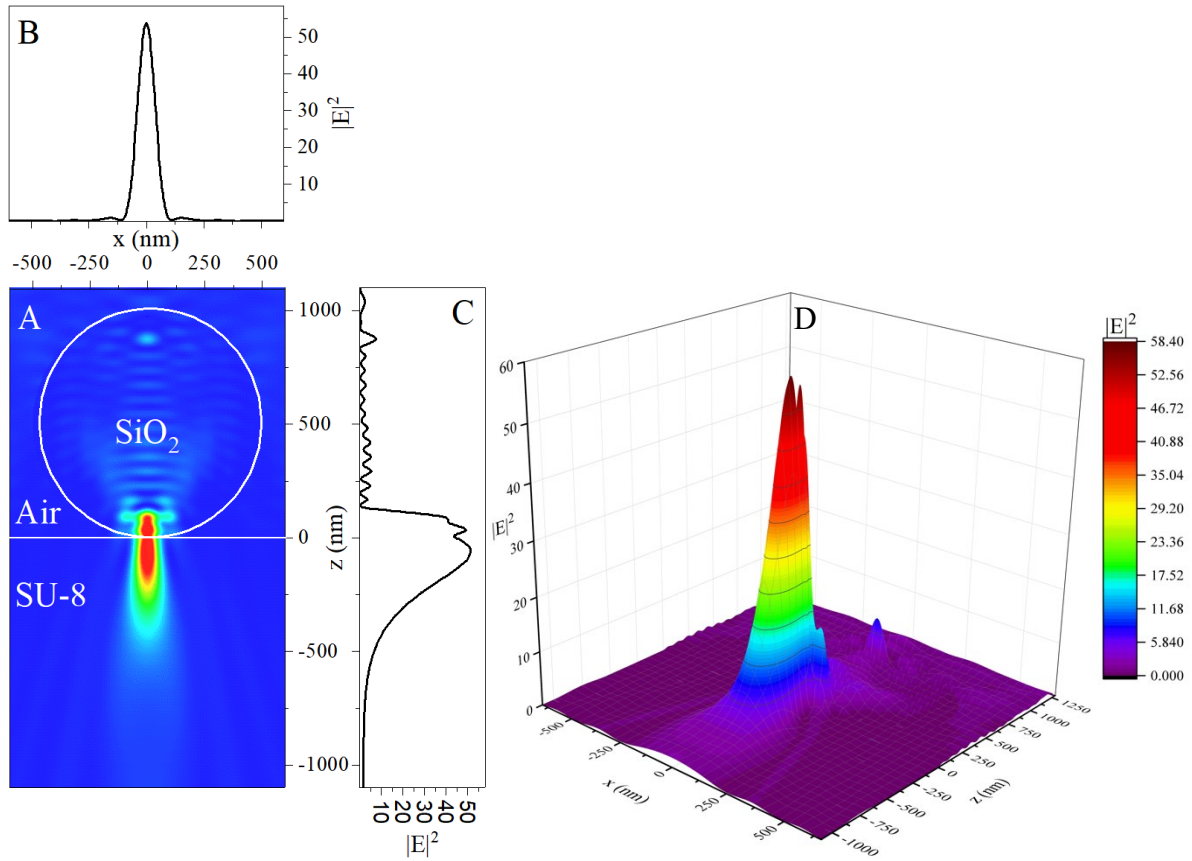


Fig. 2 (A) Simulated intensity distribution in x - z plane for laser radiation at 193 nm propagation through a 1 μ m microsphere using linearly polarised light in the x direction and the wave propagates in the z -direction. A microsphere is positioned on a flat SU-8 surface. (B) Spatial cross-section of the simulated data through location of the peak intensity of the focussed PNJ. (C) Spatial cross-section of the peak intensity along the beam propagation direction, z . (D) 3D plot of the intensity of the focal region.

The PNJ in the x - z plane has an elongated focal region along the z -direction. The results are sometimes referred to photonic needles and results are consistent with similar observations of PNJ's [44]. From the FDTD simulations of the intensity an elliptical focal region is observed that extends 120 nm and 300 nm in the transverse and beam propagation directions respectively. The PNJ extends about 200 nm into the SU-8 and a small portion of the light is

located inside the sphere. Although not shown here the refractive index of the SiO₂ microsphere and surrounding media can be easily changed to simulate other systems. Using the corresponding refractive index for diamond for example whilst keeping all other parameters the same one observes a focal region located deep inside the microsphere.

5.0 Temperature Calculations of SU-8

Temperature calculations provide useful information for analysing dimple formation mechanisms. Electric field enhancement at the sphere-substrate interface manifests in an increased temperature of the SU-8 film. Temperatures of SU-8 when subjected to 193 nm laser radiation have been investigated both analytically and using COMSOL MultiPhysics™ FEM software. FEM and analytical calculations can be used to predict temperature rises in both the spatial and temporal domains. For analysis purposes, we estimate the temperature rise analytically in the SU-8. The solution used assumes a Gaussian spatial heat source beneath the microsphere and a time dependent laser pulse of the form:

$$I_0(t) = \frac{\Phi t}{t_l^2} \exp\left[-\frac{t}{t_l}\right] \quad (15)$$

where t_l is defined such that the FWHM laser pulse corresponds to 12 ns and Φ is the laser fluence. Initially we calculate the temperature of the SU-8 layer using a closed form solution to the 3D heat equation [37].

$$T(r, z, t) = S_0 \frac{A_0 \alpha_A}{C_s \rho_s} \int_0^t dt_1 I_0(t-t_1) \frac{\exp\left(-\frac{r^2}{r_0^2 + 4\chi t}\right)}{1 + \frac{4\chi t_1}{r_0^2}} F(z, t_1) \quad (16)$$

where S_0 is the optical enhancement factor, $r_0 = (x_0, y_0)^{1/2}$ is the width of corresponding Gaussian beam, r is the radial coordinate, α_A is the absorption coefficient, C_s is the specific

heat capacity, ρ_s is the thermal conductivity, A_0 is the absorptivity, $\chi = k_s / C_s \rho$ is the thermal diffusivity of the SU-8 substrate, and the $F(z, t)$ is defined in equation (7).

We note that a Gaussian spatial intensity profile beneath the particle is assumed and is consistent from curve fitting a Gaussian function to the AFM cross-sectional measurements.

For comparison purposes the temperature is calculated using FEM, COMSOL MultiPhysics™ 5.3 using a 2D axis-symmetric configuration. Simulations of this nature are useful for predicting temperatures for differing laser fluences and experimental conditions. Similarly, these simulations are a useful aid for investigating material decomposition mechanisms [45]. One can calculate substrate temperatures for different laser fluences and compare results with corresponding melting and boiling temperatures. These processes are governed by the physical and optical properties of the material and light source. For solid materials over short interaction times and heat conduction is the dominant heat transfer mechanism [46]. In these simulations we use the heat equation [10]

$$\rho C_\rho \frac{\partial T}{\partial t} + \rho C_\rho U \cdot \nabla T + \nabla \cdot q = Q_s + Q_{ted} \quad (17)$$

where, ρ , is the material density, T is the material temperature, k is the thermal conductivity and C_ρ , is the specific heat capacity. Q_s is the heat source and Q_{ted} is the thermoelastic damping term. Gaussian and quasi-Gaussian functions were used to define the spatial and temporal laser pulse. In these FEM calculations we used and experimentally measured laser pulse for the time dependent heat source. Default solver settings for heat transfer studies were used with the exception of the time step which was set to strict. This forces the solver to recalculate at each of the manually defined individual time steps as well as any necessary intermediate steps.

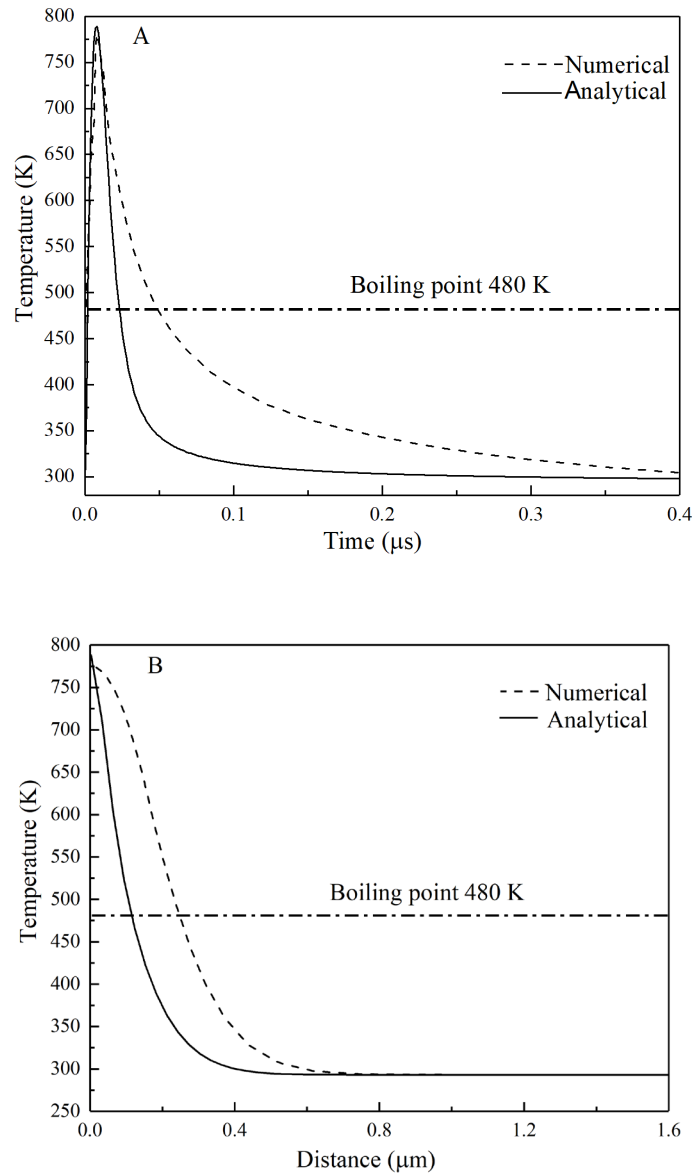


Fig. 3 Temporal (A) and spatial (B) temperature calculations of laser irradiated SU-8 at 193 nm at a fluence of $1045 \text{ J}\cdot\text{cm}^{-2}$. The horizontal dash-dot line indicates the boiling point of SU-8.

A two-layer geometry was implemented, consisting of air at the front surface of the solid SU-8 substrate. In the experiments a relatively thick $5 \mu\text{m}$ SU-8 layer was spun onto a soda lime glass microscope slide. The SU-8 thickness is much larger than the heat propagation distance and therefore to minimise computational time the supporting soda-lime glass substrate was not included in the FEM model. Both conduction and convection at the surface were used in the

simulation and radiation losses were assumed negligible. Figure 3, A and B show the temperature distribution of a SU-8 material in the time and spatial domains after being subjected to a single laser pulse. These temperature calculations were computed using a laser fluences of 1045 mJ.cm^{-2} which corresponded to the laser fluence beneath the microsphere. Although the incident laser fluence was relatively low, 45 mJ.cm^{-2} , the peak laser fluence is increased due to the focusing effect resulting in a concomitant and significant temperature rise.

6.0. Experimental

A soda-lime microscope slide was sonicated in deionized water, acetone and isopropanol for 10 min, respectively, using an ultrasound cleaner (UW ultra-wave QS5). The slide was blown dry with nitrogen gas for 2 min to remove residual solvent and left in air to cool back down to ambient temperature. SU-8 negative tone photoresist, (GM1060, Gersteltec Sarl), was spin coated (SUSS Micro Tec Lithography, DELTA 10TT) at a speed of 5,000 rpm for 30 s. The sample was left to stabilise for 40 min before placing on a hot plate. SU-8 substrates were heated using a two stages heating process, $65 \text{ }^\circ\text{C}$ for 5 min followed by $95 \text{ }^\circ\text{C}$ for 5 min and cured using a UV lamp emitting at a wavelength of 365 nm at an irradiance of 10 mW cm^{-2} . This resulted in a $5 \text{ }\mu\text{m}$ thick SU-8 layer verified using a Stylus Profilometry (DektakXT, BRUCKER) and double checked using a white light interferometer (WYKO, NT1100). A dilute solution of SiO_2 microparticles (Kisker Biotech), $1.0 \text{ }\mu\text{m}$ diameter suspended in water was deposited on the SU-8 surface substrate. The SiO_2 particles on the SU-8 layer were exposed to a single pulse from a Lambda Physik, LPX 202 ArF excimer laser emitting at a wavelength $\lambda = 193 \text{ nm}$. The pulse width was measured as $\tau = 12 \text{ ns}$ (FWHM) at a charging voltage of 26 kV (photodiode, Hamamatsu, S7911 measured using an oscilloscope, Infinium, 500 MHz, 2 GB samples s^{-1}). A stainless-steel object mask consisting of a circular aperture, 2 mm diameter, was imaged onto the SU-8 layer using a mask projection imaging set-up. The aperture was positioned in the raw laser beam to select a near-uniform laser

fluence. The laser beam was steered using dielectric mirrors optimised for reflection at 45°. A plano-convex silica lens, focal length 82 mm at 193 nm was used to image the stainless-steel mask aperture using a 1/10 magnification. Laser energy was measured after the lens to account for transmission and reflection losses. The processing set up can be found in [47]. A variable angle dual plate beam attenuator (ML2110-Metrolux, Germany) was used to control the laser fluence, and the energy was measured using a Joule meter (Molelectron). A motion control stage (Aerotech Fibre align) was used to manipulate the sample in the vicinity of the image plane. A schematic of the sample and incident laser beam is shown in figure 4. Samples were exposed to laser irradiation in air and a fume extractor positioned in close proximity to the irradiated site. After the laser experiments, the samples were characterized by Scanning Electron Microscopy, SEM (Zeiss EVO60) and Atomic Force Microscope AFM (Bruker edge).

7.0 Results and Discussion

Figure 4 shows an illustration of the sample orientation relative to the laser beam.

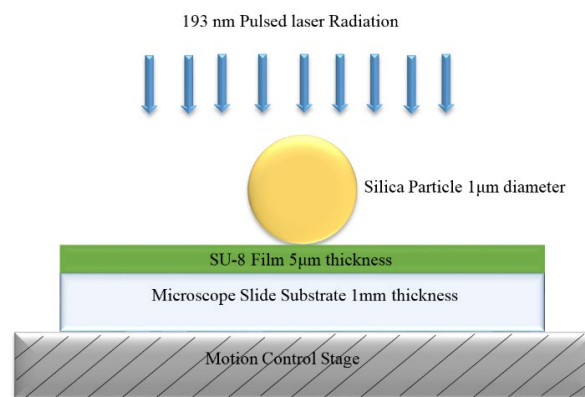


Fig. 4. Schematic of a silica particle 1µm diameter in near contact with an SU-8 layer of thickness 5 µm. Note the thickness of the SU-8 is not drawn to scale. A single pulse from an ArF 193 nm laser was used to couple light into the microsphere to focus light into the underlying SU-8 substrate.

Figure 5A shows an SEM image of a typical SiO₂ microsphere used in the experiments 5B shows an AFM measurement of the surface-modified SU-8 layer. The microsphere is 1 μm in diameter and has a back focal length $f_{BFL}=190$ nm and a corresponding effective focal length of 590 nm.

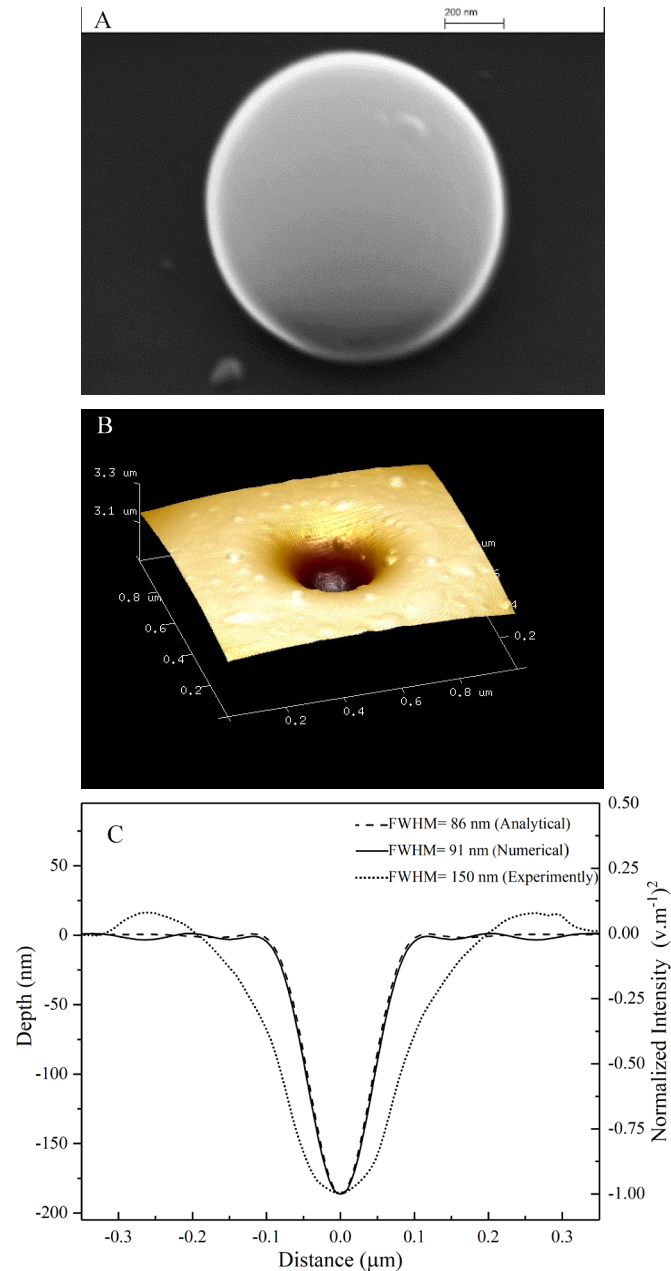


Fig. 5. (A) SEM image of a 1 μm silica microsphere on an SU-8 substrate. (B) AFM image of the dimple structure formed on an SU-8 substrate using a single laser pulse from an ArF laser, wavelength 193 nm, at an incident laser fluence of 45 mJ.cm⁻² (1045 mJcm⁻² after focussing). (C) Spatial cross-section of the dimple structure. The curves

represent the normalised intensity calculation using R-W equations, normalised intensity distribution calculated by FDTD and the AFM cross-sectional profile taken through the centre of dimple structure (depth 180 nm). The analytical and numerical data have been inverted to compare with the dimple cross-section.

A dilute solution of silica particles was used so that a single microsphere could be irradiated at 193 nm. Although, we have no surface roughness data for the microspheres used in these experiments one assumes optical scattering was relatively low as the electric field has been tightly confined. This is evident from the spatial cross-sectional profile obtained from atomic force measurements of the dimple feature, see figures 5B,C. Figure 5C compares experimental cross-sectional spatial profile with that of numerical and analytical results of the intensity in the focal region. Numerical and analytical results were inverted and plotted alongside the cross-sectional spatial profile of the dimple feature. Assuming a circularly symmetric Gaussian focal region the mass of SU-8 removed corresponds to $7.6 \pm 0.1 \times 10^{-9}$ g and a volume of $6.3 \times 10^{-3} \mu\text{m}^3$. From observations one observes a dimple size that is larger than both the numerical and analytical intensity profiles. This can be reconciled as being due to the temperature of SU-8 rising above its boiling point (480 K). Species will inevitably be transported away from the dimple region at temperatures above their boiling point. Transportation mechanisms may consist of a combination of evaporative and ablative processes. However, in this work we have not tried to deconvolve and quantify these two different mechanisms. We note that because of the optical field enhancement the surface modification was realised in SU-8 using a relatively low incident laser fluence of $45 \text{ mJ}\cdot\text{cm}^{-2}$. Beneath the microsphere the incident laser fluence is considerably higher at $1045 \text{ mJ}\cdot\text{cm}^{-2}$ which is considerably higher than the laser ablation threshold of SU-8 [48]. After the end of the laser pulse, 12 ns FWHM, the temperature of the dimple walls remain momentarily higher than the boiling point of SU-8 further contributing to mass transport and growth of the dimple

feature. A lower and (higher) laser incident laser fluence could be used to realise more subtle and (deeper) surface relief features.

It is informative to consider the mechanism of microsphere ejection. The microsphere ejection mechanism is quite complex as there may be several contributing mechanisms taking place simultaneously. At risk of over simplifying the ejection mechanism we estimate the displacement and acceleration of the SU-8 substrate using equations (4) and (5). Magnitudes of the displacement correspond to $H \approx 280$ nm and a corresponding acceleration of $a = 2.117 \times 10^9$ m s⁻². Due to the high acceleration we assume that the accelerating substrate provides a significant contribution to the ejection of the microsphere. A more representative estimate of the surface displacement can be calculated by taking into consideration the temporal profile of the laser pulse, see equation 6. From these calculations a smaller magnitude of the acceleration is calculated $\sim 1.89 \times 10^9$ m s⁻² [36, 47]. Both calculations of the acceleration are very much higher than that posed by gravity. We note that we have not considered any contribution forces from evaporative and ablative species escaping from beneath the microsphere but these effects may contribute to the microsphere ejection mechanism.

8.0 Conclusion

In summary, we report laser processing of SU-8 using a PNJ emitting at a wavelength of 193 nm to realise small sub-wavelength dimple shaped cavity. The dimple measures 150 nm in size at the FWHM point. The SiO₂ microsphere acts as a small ball lens that tightly focuses laser radiation. As a consequence, 193 nm laser radiation locally heats SU-8 above its boiling point in the region beneath the microsphere. FDTD simulations provide a useful information about PNJ's spatial extent and as such the simulations can be used to engineer the position and geometry of a PNJ. We note that PNJs can be realised from other refracting elements that are not necessarily spherical and work in this area is ongoing. Similarly, surface modification

need not be restricted to planar surfaces. Work is presently underway to couple laser radiation into microspheres and nanospheres in contact with biological cells. Utilization of subwavelength photonic PNJs may open up novel opportunities within the biomedical field to controllably disrupt cell membranes for drug delivery and transfection studies.

Acknowledgements.

The authors acknowledge the Ministry of Higher Education & Scientific Research, Iraq, for supporting Qassim A. Al-Jarwany to study for a PhD at the University of Hull. We are grateful to the Iraqi Cultural Attaché, London, for their support. In addition, our gratitude to Mr Timothy Dunstan for his help with the SEM measurements.

References

- [1] Khosrofian JM, Garetz BA. Measurement of a Gaussian laser beam diameter through the direct inversion of knife-edge data. *Appl Opt* 1983;22:3406. doi:10.1364/AO.22.003406.
- [2] Suresh P, Mariyal C, Gokulakrishnan K, Rajesh KB, Pillai TVS. Tight focusing of circularly polarized beam over high NA lens axicon with a diffractive optical element. *Optik (Stuttg)* 2013. doi:10.1016/j.ijleo.2013.01.060.
- [3] van Oerle BM, Schaich TJ, Godfried HP, Kriele PAC, Houwman EP, Nelissen WGM, et al. High NA diamond lenses for near field optical data storage. *Ind Diam Rev* 2006.
- [4] de Araújo MA, Silva R, de Lima E, Pereira DP, de Oliveira PC. Measurement of Gaussian laser beam radius using the knife-edge technique: improvement on data analysis. *Appl Opt* 2009;48:393. doi:10.1364/AO.48.000393.
- [5] Sheik-Bahae M, Said AA, Wei TH, Hagan DJ, Van Stryland EW. Sensitive Measurement of Optical Nonlinearities Using a Single Beam. *IEEE J Quantum Electron* 1990;26:760–9. doi:10.1109/3.53394.
- [6] Baesso ML, Shen J, Snook RD. Mode-mismatched thermal lens determination of temperature

- coefficient of optical path length in soda lime glass at different wavelengths. *J Appl Phys* 1994;75:3732–7. doi:10.1063/1.356045.
- [7] Xiong R, Samal SK, Demeester J, Skirtach AG, De Smedt SC, Braeckmans K. Laser-assisted photoporation: fundamentals, technological advances and applications. *Adv Phys X* 2016;1:596–620. doi:10.1080/23746149.2016.1228476.
- [8] Wen Y, Wang F, Yu H, Wang Y, Liu L, Li WJ. Submicron processing using laser-induced photonic nanojet. *2017 IEEE 17th Int Conf Nanotechnology, NANO 2017* 2017;2:940–1. doi:10.1109/NANO.2017.8117311.
- [9] Wen Y, Wang F, Yu H, Li P, Liu L, Li WJ. Laser-nanomachining by microsphere induced photonic nanojet. *Sensors Actuators, A Phys* 2017. doi:10.1016/j.sna.2017.03.009.
- [10] Wang XC, Zheng HY, Tan CW, Wang F, Yu HY, Pey KL. Fabrication of silicon nanobump arrays by near-field enhanced laser irradiation. *Appl Phys Lett* 2010. doi:10.1063/1.3327513.
- [11] Wysocki G, Denk R, Piglmayer K, Arnold N, Bäuerle D. Single-step fabrication of silicon-cone arrays. *Appl Phys Lett* 2003. doi:10.1063/1.1538347.
- [12] Shakhov A, Astafiev A, Gulin A, Nadochenko V. Femtosecond Nanostructuring of Glass with Optically Trapped Microspheres and Chemical Etching. *ACS Appl Mater Interfaces* 2015. doi:10.1021/acsami.5b09454.
- [13] Wang ZB, Guo W, Pena A, Whitehead DJ, Luk'yanchuk BS, Li L, et al. Laser micro/nano fabrication in glass with tunable-focus particle lens array. *Opt Express* 2008;16:19706. doi:10.1364/OE.16.019706.
- [14] McLeod JH. The Axicon: A New Type of Optical Element. *J Opt Soc Am* 1954. doi:10.1364/JOSA.44.000592.
- [15] Li Y, Xin H, Liu X, Zhang Y, Lei H, Li B. Trapping and Detection of Nanoparticles and Cells Using a Parallel Photonic Nanojet Array. *ACS Nano* 2016;10:5800–8. doi:10.1021/acsnano.5b08081.

- [16] Ferreira M, Gomes A, Kowal D, Statkiewicz-Barabach G, Mergo P, Frazão O. The Fiber Connection Method Using a Tapered Silica Fiber Tip for Microstructured Polymer Optical Fibers. *Fibers* 2018;6:4. doi:10.3390/fib6010004.
- [17] Zhang Y, Tang X, Zhang Y, Su W, Liu Z, Yang X, et al. 3-dimensional dark traps for low refractive index bio-cells using a single optical fiber Bessel beam. *Opt Lett* 2018. doi:10.1364/ol.43.002784.
- [18] Cizmar T, Garces-Chavez V, Dholakia K, Zemanek P. Optical trapping in counter-propagating Bessel beams. *Opt. Trapp. Opt. Micromanipulation*, 2004. doi:10.1117/12.557188.
- [19] Paiè P, Zandrini T, Vázquez RM, Osellame R, Bragheri F. Particle manipulation by optical forces in microfluidic devices. *Micromachines* 2018;9:1–21. doi:10.3390/mi9050200.
- [20] Yan H, Shao D, Lao YH, Li M, Hu H, Leong KW. Engineering Cell Membrane-Based Nanotherapeutics to Target Inflammation. *Adv Sci* 2019;1900605. doi:10.1002/advs.201900605.
- [21] Firester AH, Heller ME, Sheng P. Knife-edge scanning measurements of subwavelength focused light beams. *Appl Opt* 1977;16:1971–4. doi:10.1364/AO.16.001971.
- [22] Jabbar AS, Abbas SI, Al-zubaidy MH. Studying the Linear and Nonlinear Optical Properties by Using Z-Scan Technique for CdS Thin Films Prepared by CBD Technique 2018;10:7–13. doi:10.5539/apr.v10n3p7.
- [23] Skinner DR, Whitcher RE. Measurement of the radius of a high-power laser beam near the focus of a lens. *J Phys E* 1972;5:237–8. doi:10.1088/0022-3735/5/3/015.
- [24] Orlov S, Huber C, Marchenko P, Banzer P, Leuchs G. Corrected knife-edge-based reconstruction of tightly focused higher order beams 2016;517520:10896–904.
- [25] Shayler PJ. Laser beam distribution in the focal region. *Appl Opt* 1978;17:2673–4. doi:10.1364/AO.17.002673.

- [26] Chapple PB. Beam waist and M2 measurement using a finite slit. *Opt Eng* 1994;33:2461–6. doi:10.1117/12.169739.
- [27] Dimens N. An overview of scanning near-field optical microscopy in characterization of nano-materials 2014;5:203–12.
- [28] Ashkin A, Dziedzic JM, Yamane T. Optical trapping and manipulation of single cells using infrared laser beams. *Nature* 1987. doi:10.1038/330769a0.
- [29] Jacob J Stamnes. *Waves in Focal Regions Propagation, Diffraction and Focussing of light*, Sound and Water Waves. Bristol: 1986.
- [30] Ignatowsky W. Diffraction by a lens having arbitrary opening. *Trans Opt Int Petrogr* 1919.
- [31] v. Ignatowsky W. Diffraktion und Reflexion, abgeleitet aus den Maxwell'schen Gleichungen. *Ann Phys* 1908. doi:10.1002/andp.19083311012.
- [32] Richards B, Wolf E. Electromagnetic Diffraction in Optical Systems. II. Structure of the Image Field in an Aplanatic System. *Proc R Soc A Math Phys Eng Sci* 1959;253:358–79. doi:10.1098/rspa.1959.0200.
- [33] Wolf E. Electromagnetic Diffraction in Optical Systems. I. An Integral Representation of the Image Field. *Proc R Soc A Math Phys Eng Sci* 1959;253:349–57. doi:10.1098/rspa.1959.0199.
- [34] A V Kharitonov SSK. Strong focusing higher-order laser modes : transverse and longitudinal optical fields 2015. doi:10.1088/1742-6596/613/1/012010.
- [35] Lerman GM, Levy U. Effect of radial polarization and apodization on spot size under tight focusing conditions. *Opt Express* 2008.
- [36] Tam AC, Leung WP, Zapka W, Ziemlich W. Laser-cleaning techniques for removal of surface particulates. *J Appl Phys* 1992;71:3515–23. doi:10.1063/1.350906.
- [37] Luk'yanchuk BS, Arnold N, Huang SM, Wang ZB, Hong MH. Three-dimensional effects in dry laser cleaning. *Appl Phys A* 2003;77:209–15. doi:10.1007/s00339-003-2139-z.

- [38] Bäuerle D. *Laser Processing and Chemistry*. vol. 1542. 4th ed. Austria: Springer Heidelberg Dordrecht London New York; 2011. doi:10.1017/CBO9781107415324.004.
- [39] Micheletto R, Fukuda H, Ohtsu M. A Simple Method for the Production of a Two-Dimensional, Ordered Array of Small Latex Particles. *Langmuir* 1995;11:3333–6. doi:10.1021/la00009a012.
- [40] Münzer HJ, Mosbacher M, Bertsch M, Zimmermann J, Leiderer P, Boneberg J. Local field enhancement effects for nanostructuring of surfaces. *J Microsc* 2001;202:129–35. doi:10.1046/j.1365-2818.2001.00876.x.
- [41] Sedao X, Derrien TJY, Romer GRBE, Pathiraj B, Huis In 'T Veld AJ. Large area laser surface micro/nanopatterning by contact microsphere lens arrays. *Appl Phys A Mater Sci Process* 2013;111:701–9. doi:10.1007/s00339-013-7651-1.
- [42] Kitamura R, Pilon L, Jonasz M. Optical constants of silica glass from extreme ultraviolet to far infrared at near room temperature. *Appl Opt* 2007;46:8118. doi:10.1364/AO.46.008118.
- [43] Feng R, Farris RJ. Characterization of optical properties of SU-8 and fabrication of optical components. *J Micromechanics Microengineering* 2003;13:80–8. doi:10.1088/0960-1317/13/1/312.
- [44] Darafsheh A, Bollinger D. Systematic study of the characteristics of the photonic nanojets formed by dielectric microcylinders. *Opt Commun* 2017;402:270–5. doi:10.1016/j.optcom.2017.06.004.
- [45] Brown MS, Arnold CB. *Fundamentals of Laser-Material Interaction and Application to Multiscale Surface Modification*. vol. 135, 2010, p. 91–120. doi:10.1007/978-3-642-10523-4.
- [46] Guo Q, Ahmed S. COMSOL Simulation Application for Thermoplastics Viscosity Measurement 2016:2–6.
- [47] Mohammed AF, Al-Jarwany QA, Clarke AJ, Amaral TM, Lawrence J, Kemp NT, et al. Ablation threshold measurements and surface modifications of 193 nm laser irradiated 4H-SiC.

Chem Phys Lett 2018;713:194–202. doi:10.1016/j.cplett.2018.09.057.

- [48] Pedder JEA, Holmes AS. A Study of Angular Dependence in the Ablation Rate of Polymers by Nanosecond Pulses. Phot Process Microelectron Photonics V 2006;6106:286–94. doi:10.1117/12.659793.
- [49] Mittal KL, Lei WS. Laser technology: Applications in adhesion and related areas. 2017. doi:10.1002/9781119185031.